APPLIED SCIENCES AND ENGINEERING

Self-adaptive virtual microchannel for continuous enrichment and separation of nanoparticles

Yang Yang[1], Lin Zhang[2], Ke Jin[1], Meihang He[1], Wei Wei[1], Xuejiao Chen[1], Qingrui Yang[1], Yanyan Wang[1], Wei Pang[1], Xiubao Ren[2], Xuexin Duan[1]*

The transport, enrichment, and purification of nanoparticles are fundamental activities in the fields of biology, chemistry, material science, and medicine. Here, we demonstrate an approach for manipulating nanospecimens in which a virtual channel with a diameter that can be spontaneously self-adjusted from dozens to a few micrometers based on the concentration of samples is formed by acoustic waves and streams that are triggered and stabilized by a gigahertz bulk acoustic resonator and microfluidics, respectively. By combining a specially designed arc-shaped resonator and lateral flow, the in situ enrichment, focusing, displacement, and continuous size-based separation of nanoparticles were achieved, with the ability to capture 30-nm polystyrene nanoparticles and continuously focus 150-nm polystyrene nanoparticles. Furthermore, exosome separation was also demonstrated. This technology overcomes the limitation of continuously manipulating particles under 200 nm and has the potential to be useful for a wide range of applications in chemistry, life sciences, and medicine.

INTRODUCTION

Nanoparticles are currently one of the most studied branches of science and technology and have numerous applications in biomedical, chemical, optical, and electronic fields (*1*–*6*). They can be roughly divided into "soft particles" [such as liposomes, viruses, DNA nanoballs, and extracellular vesicles (EVs)] and "hard particles" (such as metals, metal oxides, and semiconductor nanoparticles). Bionanoparticles are often "soft," and they have received considerable research attention over the past decade because of their unique biological functions and features. For example, synthesized liposomes (~100 nm) and purified viruses (50 to 300 nm) have been widely used as drug delivery carriers (*7*), constructed DNA nanoballs (120 to 250 nm) have been used as basic units for high-throughput DNA sequencing (*8*), and exosomes (30 to 150 nm), a kind of EV, are believed to play important roles in intercellular communication and potential biomarkers for in vitro diagnoses (*9*–*11*). The manipulation of nanoparticles, including extraction, enrichment, and separation, is an essential requirement for downstream applications. For example, homogeneous nanoparticles are preferred drug carriers because of their long blood circulation times, while nanoparticles with wide size distributions may cause unintended cytotoxic effects (*12*–*14*). Different sized EVs have been reported to carry different genomic and protein compositions, which have distinct biological functions (*15*–*17*). Currently, density gradient centrifugation (*18*, *19*), membrane filtration (*20*–*22*), and size exclusion chromatography (*18*) are the standard methods for enriching and separating bionanoparticles. However, a minimum sample volume is generally required in these bulk approaches, which could be difficult for rare biological or medical samples. In addition, because of the soft nature of nanoparticles, they are prone to clogging, damage, and loss during contact-based and multistep treatments (*23*). Miniaturized microfluidic devices, which operate at the micrometer scale, have been demonstrated to be effective tools for manipulating nanoparticles, especially in small-volume samples (*24*–*26*). Because of the relatively low Reynolds numbers (laminar flow) in these systems, a homogeneous force field and steady flow conditions are well maintained throughout the process, allowing for separated nanoparticles with higher purities and yields than bulk methods. In general, microfluidic methods can be classified as passive approaches, which use sheath fluids to pinch suspended particles at specific positions in the channel, or active approaches, which use external forces to drive particles laterally to their equilibrium positions.

Despite great promise, no commercially available microfluidic systems for nanoparticle isolation and enrichment are currently available (*27*). Current microfluidics-based nanoparticle manipulations face several major challenges: (i) Microfluidic devices are still too large to manipulate particles smaller than 100 nm. When the particle size is reduced to the submicrometer scale, particle movement is often dominated by the drag forces induced by fluid motion and Brownian motion. Thus, it is more difficult to manipulate the particles with inertial fluids or external force fields. In principle, scaling down the dimensions of the microfluidic channel to submicrometer levels could be a solution for improving their manipulation ability. For example, nanofluidic devices (*28*, *29*), such as nanoscale deterministic lateral displacement (*30*), have been used to detect and manipulate sub-100-nm bioparticles. However, the enhanced interactions between the nanoparticles in such limited space induce uncontrolled agglomeration, adhesion, and even damage to the bioparticles. In addition, the high flow resistance at the submicrometer scale limits the throughput of the method, and channel blockages frequently occur. (ii) It is difficult to develop a "one size fits all" microfluidic system that can handle different nanoparticles. Bionanoparticles are often found in complex mixtures with varying physiochemical properties. Their compositions and concentrations differ as well. For example, EVs are composed of lipid bilayers, proteins, and various RNAs, and their concentrations have been reported to vary by several orders of magnitude in different clinical samples (*23*). Common strategies for solving these issues include optimizing the buffer conditions by introducing additives or diluting the original samples, as in viscoelastic or inertial fluidics (*31*), or using tunable external fields, such as magnetic (*4*), electric

[1]State Key Laboratory of Precision Measuring Technology and Instruments, Tianjin University, Tianjin 300072, China. [2]Tianjin Medical University Cancer Institute & Hospital, Tianjin 300072, China.
*Corresponding author. Email: xduan@tju.edu.cn

(*32*), optical (*33*), and acoustic fields (*34*, *35*). Regardless of whether the approach is passive or active, the parameters optimized for one type of sample at a specific concentration cannot be easily applied to others; thus, it is difficult to establish standard operating procedures. This severely limits the use of microfluidic devices for automatic particle manipulations of unknown samples. The ideal technology would be (i) compatible with different buffers without additives, (ii) tolerant of different types and concentrations of samples without being affected by their interactions or triggering agglomerates, and (iii) capable of maintaining both operational efficiency and throughput. Acoustofluidics (the fusion of acoustics and microfluidics) is a potential candidate for approaching this goal. Combining the characteristics of acoustic waves, which do not have strict requirements for buffer composition and good compatibility with other external fields, and the powerful handling ability of acoustic streams gives acoustofluidics unique advantages in nanoparticle manipulation (*23*, *24*, *34*–*38*). The most common strategies for generating acoustic streams include increasing the resonant frequency (*39*, *40*) and introducing a microstructure (sharp edges or bubbles) (*41*, *42*) that causes a pair of symmetrical acoustic vortices to form in the flow plane. However, this feature ensures that the effects of acoustic streaming and lateral flow are coupled on the same plane, which limits the compatibility and performance of this technology.

To solve these issues, we present a novel acoustofluidic approach for nanoparticle manipulation that uses a specially designed fan-shaped acoustic device (Fig. 1). A series of closed and connected microvortices are triggered by the ultrahigh-frequency bulk acoustic wave (UHF BAW) and confined by microfluidics, which form a virtual channel. The high-speed rotating microvortices generate strong drag forces, facilitating small particle manipulations. The target nanoparticles could be efficiently dragged and hydrodynamically confined within the virtual channel and further displaced by lateral flow. The unique vibration mode and device design place the plane of the acoustic vortices orthogonal to the lateral flow, maximizing the focusing ability. As the channel is virtual and there is no real microstructure, the clogging of the channel and damage of the bioparticles induced by solid structures, such as filter or pillar, are completely avoided. The trapping status of the nanoparticles is mainly controlled by the dynamic balance between the particle interactions and the acoustic and hydrodynamic fields; thus, the inner diameter (ID) of the virtual channel could be self-adjusted for different amounts of nanoparticles without changing any flow parameters. In this work, we report the design principle and optimization of the acoustic device and the virtual channel. The enrichment, focusing, and displacement of nanoparticles with sizes as small as dozens of nanometers were achieved. The ID of the virtual channel was demonstrated to spontaneously adjust from a few micrometers to tens of micrometers to adapt to different sample concentrations. In terms of particle focusing–type enrichment, the recovery efficiency of the 300-, 200-, and 150-nm polystyrene (PS) particles reached 92.6, 85.6, and 54.5%, respectively. Exosomes less than 150 nm were directly purified from plasma to verify the performance and biocompatibility of the system. Benefited by the flexible acoustic and hydrodynamic features, the developed self-adaptive virtual microchannel provides a new universal microfluidic strategy for handling complicated nanoparticle samples.

RESULTS

Working mechanism and device design

A schematic of the virtual microchannel system is shown in Fig. 1A. A specially designed fan-shaped ultrahigh-frequency bulk acoustic wave (UHF BAW) resonator was integrated into the microfluidic channel between one inlet and three outlets, with the symmetrical arc edges of the device gradually narrowing along the flow direction and the focal point of the device facing the center outlet. The high resonant frequency of the BAW device reduced the attenuation length of the acoustic waves and greatly increased the body force, resulting in strong acoustic streaming effects without the formation of standing waves in the *Z* direction. Because of the thickness extension vibration mode, a highly localized array of rapidly rotating enclosed three-dimensional (3D) microvortices is triggered along the edge of the

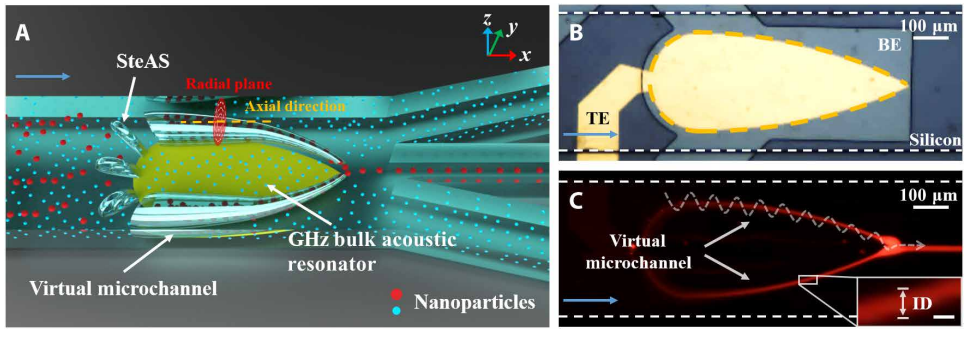

Fig. 1. Mechanism of the SteAS platform. (**A**) Schematic of nanoparticle separation based on the virtual microchannel. The platform consists of a gigahertz BAW resonator and a microfluidic channel. The SteAS is triggered by a gigahertz BAW resonator and confined in a microchannel, forming two virtual channels composed of a series of acoustic vortices. Driven by lateral flow, the mixed nanoparticles enter the channel. The large nanoparticles (red spheres) are focused and enriched by the acoustic vortices and then released from a fixed site (the vertex of the BAW device) and recovered, while the small nanoparticles (blue spheres) remain in the original uniform dispersion state. The radial plane (the plane of acoustic streaming vortices) and the axial direction (the direction of lateral flow) are represented by a red circle and a yellow dash, respectively. (**B**) Actual image of an actual gigahertz BAW device integrated with a microchannel. The zone of the bottom electrode (gray), the top electrode (yellow), and silicon substrate (dark gray) are highlighted as "BE," "TE," and "Silicon." The overlap area of BE and TE is the vibration zone of the UHF BAW device, which is represented by the yellow dashed arc. The blue arrow shows the direction of flow. (**C**) Focusing of fluorescent PS nanoparticles (300 nm) in a symmetrical virtual microchannel pointed by white arrows. The trajectories of the nanoparticles are highlighted by a white dashed spiral curve. The ID of the virtual channel is shown in the detailed image. Scale bar, 10 μm. The direction of lateral flow is pointed by the blue arrow.

acoustic device in the cross-sectional plane, which we refer to as the "stereo acoustic stream" (SteAS) (*43*, *44*). The chip is consisted of the UHF BAW device and microfluidics. The silicon substrate (dark gray), bottom electrode (gray), and top electrode (yellow) are highlighted as "Silicon," "BE," and "TE," respectively, as shown in Fig. 1B. Because the rotation axis of these vortices is parallel to the substrate, they connect and generate a virtual channel, whose shape is defined by the shape of the BAW device. Under continuous flow conditions, the particles migrate downstream with the lateral flow while being confined inside the arc-shaped virtual channel until they are released from the focal point, as shown in Fig. 1C. The ID of the virtual microchannel is defined by the boundary of focused nanoparticles, as shown in the detailed image in Fig. 1C. When this was combined with multiple outlets, focusing-type particle enrichment could be achieved. In terms of particle separation, as the focusing effect is strongly related to the particle size, larger particles (red spheres) were trapped in the SteAS and eventually released from the focal point, while smaller particles (blue spheres) were not affected. The process was similar to particles passing through a tapered channel with walls made of a membrane filter, where particles smaller than the pore size were unaffected, while larger particles were enriched. It is worth emphasizing that since the virtual channel was caused by the active SteAS, the "pore size" and "ID" can be dynamically adjusted; thus, it is more flexible for targets of different sizes.

First, we discussed the design of the BAW device. The shape of the acoustic device is the core of this system. As mentioned above, the acoustic streaming vortices are distributed along the edge of the device and follow the shape of the device. In our previous works, pentagonal structured devices were mainly used because of the device performance (quality factor, minimized spurious mode, etc.) (*43*, *45*, *46*). However, the pentagonal structure determines that the axis of the acoustic vortices must be orthogonal to the direction of the lateral flow, which causes the lateral flow and the acoustic stream to interact. Such interactions suppress the range of the acoustic stream and decrease the drag efficiency of the stream. To show the different interaction states of acoustic streaming and lateral flow, including both perpendicular and parallel, we introduced a 3D simulation model, where a square-shaped acoustic device was placed in the center of a microchannel, as shown in fig. S1. The outline of the device, parallel acoustic streaming (streaming-1), and perpendicular acoustic streaming (streaming-2) are represented by a yellow dashed square, red dashed ovals, and green dashed ovals, respectively. The simulation results for flow rates of 0 and 0.1 m/s are shown in fig. S1 (A and B, respectively). Figure S1 (C and D) shows the vortex morphologies of acoustic streaming-1 and streaming-2 under static and laminar flow, respectively. The morphology of streaming-1 is the typical state of acoustic streaming induced by sharp edges, bubbles, and high-frequency surface acoustic waves (SAWs), where the radial plane of streaming vortices (*y*-*z* plane) is parallel with the lateral flow (*y* axis) (*39*, *41*, *47*), while the morphology of streaming-2 is the state of acoustic streaming in our work, where the radial plane of streaming vortices (*x*-*z* plane) is perpendicular to the lateral flow. The streaming vortex zones are represented by black dashed circles. Figure S1 (C and D) demonstrates that streaming-1 and streaming-2 have the same morphologies and streaming vortex zone in the static state. In the lateral flow state, streaming-1 directly interacts with lateral flow so that the streaming vortex zone is suppressed, which degrades the action range and performance of acoustic streaming, while in the case of streaming-2, the lateral flow only changes the time that the particles experience the streaming, and it does not affect the morphologies of the streaming vortices. Thus, the acoustic streaming can always work in the best state. In addition, there are marked changes in the stream intensity at each vertex of the polygon, which has a negative impact on the stability of the manipulation. In this work, we aimed to develop a SteAS with a continuous operation mode and an improved performance. The key considerations of the device design were the relative spatial distribution of the vortices along the lateral flow and the continuity of the SteAS. The former maximizes the focusing performance, while the latter ensures the stability of the particle displacement in the virtual channel. Here, a fan-shaped BAW device (Fan-BAW) is proposed (Fig. 1B). The main boundary of the vortices was parallel to the lateral flow, which ensured that the radial plane of the acoustic vortices was orthogonal to the lateral flow; thus, the acoustic vortices and the lateral flow did not interact. The arc shape ensures that the SteAS forms an unobstructed virtual channel, which guarantees that the focused nanoparticles migrate smoothly. The unique shape design maximizes particle focusing while minimizing the negative impact of the lateral flow. The fabrication process of Fan-BAW is complementary metal-oxide semiconductor (CMOS) compatible, allowing for mass production (*43*, *44*, *48*). The photo of the setup, the structure of the BAW device, and the frequency response diagram are shown in figs. S2 and S3. More details about the structure of the UHF BAW device can be found in Materials and Methods.

Finite element simulation was used to design and improve our understanding of the virtual channel. Figure 2A shows the focusing process in the radial plane of the vortices without lateral flow. When particles reach the SteAS area, due to the action of the drag force (F_{drag}) and the radiation force (F_{rad}) induced by the acoustic streams and the BAWs, respectively, they are focused into the center of the SteAS via a spiral trajectory. F_{drag} drives the particles to rotate in the radial plane, while F_{rad} pushes the particles away from the device. During each rotation cycle, the particles are only affected by the acoustic radiation force when they are above the device. F_{rad} weakens as the particles move away from the device due to the attenuation of the traveling acoustic waves. The equilibrium position is the point where the acoustic pressure is not strong enough to drive on the nanoparticle, which occurs at the boundary of the virtual channel. The region surrounded by the equilibrium position is the focusing area. Since F_{rad} is proportional to the particle volume (*40*, *46*), the diameter of the virtual channel depends on the size of the nanoparticles. There is no "wall" to restrict the movement of extremely small nanoparticles that cannot be driven by F_{rad}. Figure 2B and movie S1 show the simulation results of the vibration mode and range of the 2-GHz Fan-BAW in thickness extension mode. Acoustic waves with a higher resonant frequency generate stronger acoustic streams and attenuate more rapidly (*46*). The decay length of a BAW at 2 GHz is approximately 10.4 μm in water, which provides theoretical support for the generation of strong and highly confined acoustic streaming vortices.

The distribution of the SteAS was then calculated and simulated by finite element simulation. The 3D simulation results are shown in Fig. 2 (C and D). The radial plane of the SteAS is orthogonal to the vector of the lateral flow, and the width of the device gradually decreases along the flow direction. Because of this design, the lateral flow and acoustic stream are no longer hindered by their orthogonal arrangement. In addition, the particles can complete their migration in the virtual channel, where their intensities are more uniform because of the arc-shaped design. The equilibrium position, the adaptive range of the virtual channel, and the position of the device

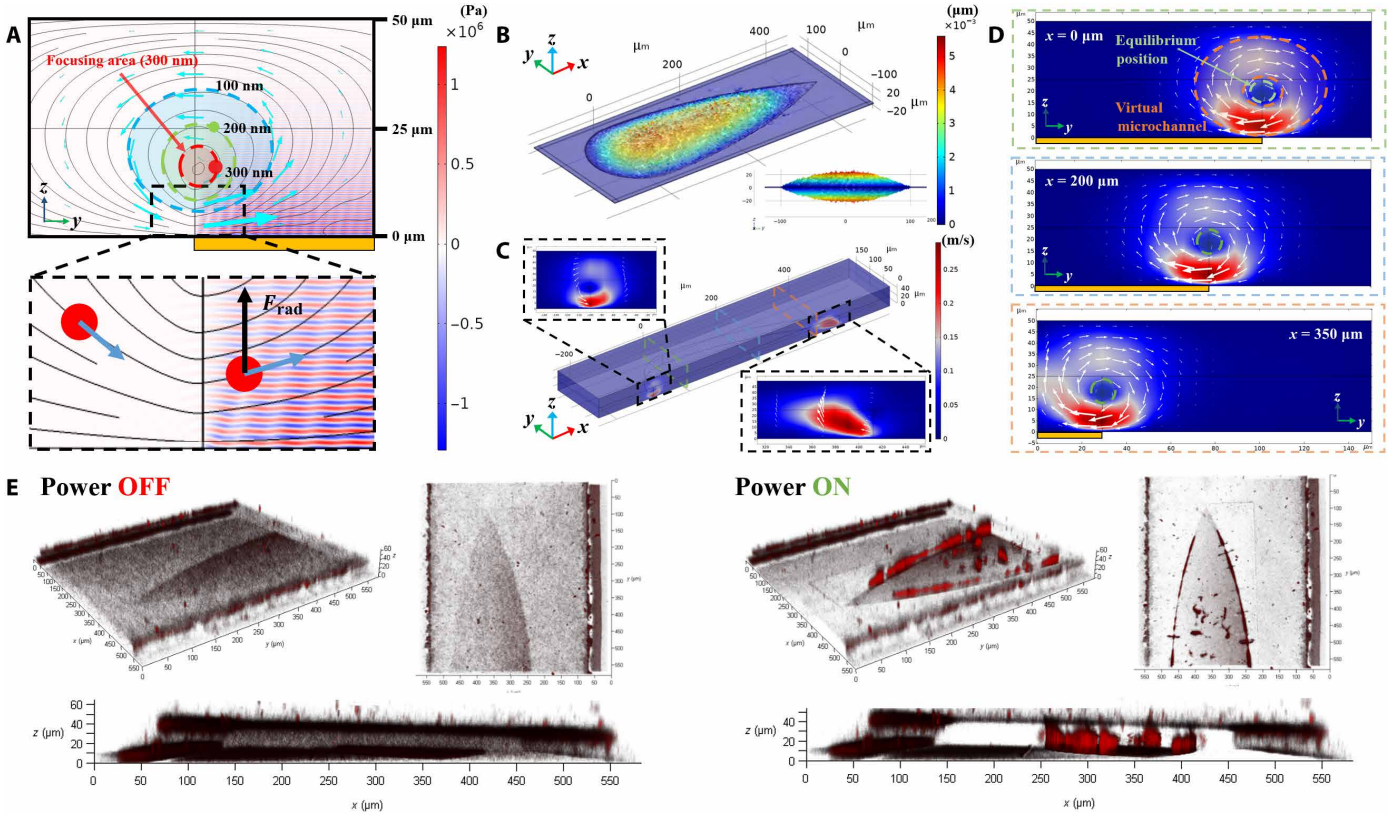

Fig. 2. Design and test of the Fan-BAW device. (**A**) Force analysis of SteAS-based focusing. The nanoparticles are focused into the center of the vortices due to F_{rad} (black arrows) and F_{drag} (blue arrows). The schematic shows the focusing area (ID of the virtual channel) for 300-nm (red), 200-nm (green), and 100-nm (blue) nanoparticles. The color surface, black curves, and cyan blue arrows represent the acoustic pressure, streamlines, and fluid vectors, respectively. The yellow rectangle indicates the position of the UHF BAW device. (**B**) 3D simulation results of the vibration mode (thickness extension mode) of the Fan-BAW device. (**C**) 3D simulation results of the distribution of acoustic vortices induced by Fan-BAWs. Detailed images show the shape of the vortex triggered by the arc edges and the vertex in the *x*-*z* plane. The slide positions ($x = 0$, 200, and 350 μm) are represented by green, blue, and orange dashed rectangles. (**D**) Distribution of the acoustic streaming vortices in different section views ($x = 0$, 200, and 350 μm). The equilibrium position, the adaptive range of the virtual channel, and the position of the device are indicated by the green dashed circles, orange dashed ring, and yellow rectangles, respectively. (**E**) 3D images of the distribution of the fluorescent nanoparticles (300 nm) before and after enrichment.

are indicated by the green dashed circles, orange dashed ring, and yellow rectangles, respectively. Two devices with slightly different shapes and sizes were included in this work and are shown in Fig. 1B and fig. S3A. To observe the 3D trapping process and the status of the enriched nanoparticles, confocal microscopy (SP8, Leica, Germany) was used to observe the motion and distribution of the nanoparticles in the virtual channel in the radial plane. Fluorescent nanoparticles (300 nm) were used to characterize the streaming trajectories and the enrichment process in an open chamber (movie S2) and a highly confined microchannel (Fig. 2E and movie S3). When the distributions of the nanoparticles before and after enrichment were compared, it is clear that the nanoparticles migrated and focused in the center of the vortices, as designed. Since the channels had no solid microstructures, this type of hydrodynamic-based and noncontact particle manipulation has good biocompatibility and can effectively avoid interface adhesion.

Height-based modulation is a unique advantage of the SteAS since it is easy to tune the channel height to adjust the equilibrium position of the virtual channel without considering the influence of standing waves, as long as the channel height is greater than 20 μm. Figure 3A illustrates the relationship between the morphology of the acoustic stream and the height of the microchannel. The adaptive boundary of the virtual microchannel, the equilibrium position, and the acoustic pressure area (defined by the decay length of acoustic waves) are represented by the orange ring, the green circle, and the red rectangle. As the height was reduced from 85 to 30 μm, the vortices became more confined without losing their strength, indicating that the trajectories of the nanoparticles approached the device, thus enhancing the effect of F_{rad}, which is reflected in the reduction of the ID of the virtual microchannel and the enhancement of the enrichment performance. To further demonstrate this phenomenon, three different sized PS nanoparticles (300, 200, and 100 nm) were used to characterize the height-controlled enrichment. To avoid movement in the axial direction, the experiments were carried out without lateral flow. Figure 3B shows that as the channel height decreased, the minimum enrichment size increased from 200 to 100 nm. Moreover, in the 200- and 300-nm results, the enrichment position migrated from the periphery to the center of the vortices due to the decrease in the ID of the virtual channel, which is consistent with the simulation results. To observe the SteAS in the radial plane, the *x*-*z*-*t* mode of confocal microscopy was used. The section view of the motion of the nanoparticles (200 nm) driven by

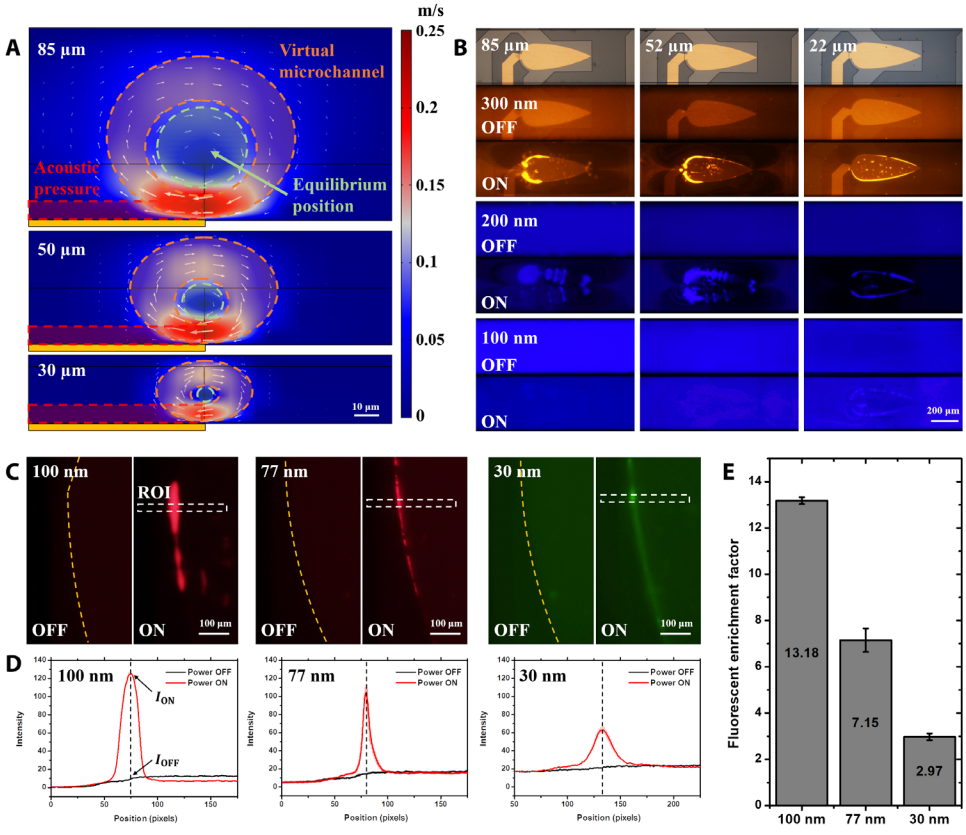

Fig. 3. Height effect and in situ enrichment. (**A**) Section view of the virtual channel formed by the SteAS with microfluidic channels of different heights. Scale bar, 10 μm. The adaptive boundary of the virtual microchannel, the equilibrium position, and the acoustic pressure area (defined by the decay length of acoustic waves) are represented by the orange ring, the green circle, and the red rectangle. The color bar represents the velocity of the stream. (**B**) Fluorescent images of the enriched PS nanoparticles (300, 200, and 100 nm) with different microchannel heights (85, 52, and 22 μm). Scale bar, 200 μm. (**C**) Fluorescent images of PS nanoparticles (100, 77, and 30 nm) before and after the in situ enrichment. The virtual microchannel is confined by a 22-μm-high microchannel. When the device is turned off, the fluorescent nanoparticles are uniformly dispersed; when the device is turned on, the nanoparticles are enriched into the virtual microchannel. The boundaries of the Fan-BAW device and ROI are marked by the yellow dashed lines and white dashed rectangles. Scale bars, 100 μm. (**D**) Fluorescent intensity of images before and after in situ enrichment in the ROI ($n = 3$). The lateral positions of the intensity peak after enrichment are marked by black dashed lines. The values of I_{ON} and I_{OFF} are pointed by black arrows. (**E**) Fluorescent enrichment factor of the in situ enrichment (100-, 77-, and 30-nm PS nanoparticles).

the SteAS is shown in movie S4. In addition, the effects of the microchannel height and the particle size were studied further, as shown in movies S5 and S6. All these results prove that adjusting the height of the microchannel is a convenient approach for confining the diameter of the virtual channel.

To test the limits on the enrichment performance of the system, 100-, 77-, and 30-nm PS nanoparticles were injected into the 22-μm-high microchannel. A low flow rate was provided by the pressure difference between the outlet and inlet to supplement the sample transportation, while the lateral flow does not have a notable impact on SteAS. By increasing the power to 1660 mW, the nanoparticles of all diameters were successfully enriched, as shown in Fig. 3C. The process of release after enrichment is shown in movie S7. The release results demonstrated that this technique can freely release the enriched nanoparticles without adhesion and aggregation, which is benefited from the noncontact and gentle hydrodynamic-based manipulation mode. To the best of our knowledge, this reaches the size limits of particle manipulation in general acoustofluidic platforms (*24*, *34*, *40*, *49*). We extracted the fluorescent intensity in the region of interest (ROI) along the width direction, as shown in Fig. 3D. The results showed that as the particle size decreases, the fluorescence intensity after enrichment decreases, and the total amount of particles enriched in the virtual microchannel, which was reflected in the integral of fluorescence intensity on the horizontal axis, also decreases. To further evaluate the enrichment performance, the fluorescent enrichment factor was introduced, which is defined by the ratio of the fluorescence intensity before (I_{OFF}) and after (I_{ON}) enrichment. The result in Fig. 3E shows that this platform has a 13.18-, 7.15-, and 2.97-fold enrichment capacity for 100-, 77-, and 30-nm PS particles, respectively.

Once the height has been fixed, the power applied to the acoustic device and the flow rate are the major tunable parameters affecting the efficiency of the SteAS. Under continuous flow conditions with a constant flow rate, the enrichment can be divided into two stages (fig. S4). The enrichment efficiency is qualitatively demonstrated by the fluorescence intensity after focusing. In the first stage, the enrichment efficiency gradually increases with increasing applied power; in the second stage, as the power increases further, the strength of the acoustic stream far exceeds the strength of the lateral flow. In this case, the enhanced acoustic stream decreases the enrichment

efficiency since excessively strong acoustic vortices deteriorate the nanoparticle release stability, which is dominated by the shear action of the lateral flow. To further investigate the relationship between the power and the flow rate, we defined a constant P^* as the applied power divided by the flow rate. The results in fig. S5 demonstrate that when P^* remains constant, the same enrichment morphology occurs, indicating that this system can adapt to different flow conditions by simply optimizing the applied power.

The concentration ranges of the particles that can be manipulated are a key factor in evaluating the compatibility of the particle manipulation platform. In particular, nanoparticles often have wide concentration ranges, such as circulating tumor cells (<10 cells/ml), blood cells (10^9 cells/ml), and exosomes (10^7 to 10^9 particles/ml). High concentrations make handling more difficult because of violent particle interactions and interface adhesion issues (*50*). As analyzed above (Fig. 2A), the size of the virtual channel is determined by the dynamic balance of F_{drag} and F_{rad}. When more particles are trapped, their balance becomes affected by particle interactions. To test the compatibility of the system with the amount of trapped particles, different concentrations of fluorescent PS nanoparticles (300 nm) were used, while the acoustic power and lateral flow parameters were kept fixed. The results of the enrichment without lateral flow are shown in fig. S6. In the absence of lateral flow, stable enrichment was achieved at all particle concentrations less than 2.5×10^{11} particles/ml. This is most likely due to the drastically increased interactions of the enriched nanoparticles in such a tightly packed virtual channel. It was also observed that the diameter of the virtual channel dynamically expanded as the amount of nanoparticles increased. This indicates that the focusing area (ID of the virtual channel) can expand/reduce spontaneously to adapt to violent/gentle particle interactions, which we call "self-adaptivity."

During continuous enrichment (Fig. 4A), the lateral flow introduced the effects of shear force and material transportation, which complicated the enrichment phenomenon. To facilitate this discussion, we divided the applied powers and concentrations into three ranges (high, middle, and low) at a fixed flow rate (1 μl/min). The effect of the applied power has been previously discussed. In general, in the low-power range, the efficiency was low due to insufficient SteAS strength, while in the high-power range, nanoparticle shedding occurred due to insufficient lateral flow; thus, the best enrichment effect can be obtained in the middle-power range. Similar to the enrichment without lateral flow, in the high-concentration range, the enrichment efficiency was low due to the interactions between the trapped nanoparticles, which resulted in the particles escaping from the virtual channel. In the middle concentration range, the ideal morphology of continuous enrichment was obtained. The low-concentration range is a unique area, which we refer to as the "in situ enrichment" area. In this area, the abundance of nanoparticles is insufficient for supporting continuous focusing and release, and the release process depends on the transport effect of the lateral flow. The nanoparticles flowing through the virtual channel are enriched in situ around the release zone highlighted by the orange dashed rectangle and continuously focused when the total amount of enriched particles reaches the loading threshold of the acoustic vortices. Because of the combined effects of the acoustic field and the particle interactions, there are multiple expanded areas; for example, in the high-concentration and high-power areas, the overloading and shedding of nanoparticles occur at the same time. To ensure the same experimental state, all experiments were done at one time after gradient dilution with the same sample and divided into 10 groups with different concentrations. Each group of samples was washed with deionized (DI) water after experiments. Then, the next group of sample was injected into the microfluidics for focusing. The experimental hardware and software conditions were strictly guaranteed in the same state to ensure the accuracy of subsequent fluorescence semiquantification.

To illustrate the stability of the enrichment, we use the enrichment process at 256× dilution as an example to demonstrate the enrichment process, as shown in fig. S7. The enrichment process is divided into two stages, the growth stage and stable stage, which are highlighted by a blue and green rectangle, respectively. During the growth stage, the total amount of trapped particles is lower than the capacity of the virtual microchannel, so the enrichment factor keeps increasing (from 1 to 5 s). When the total amount of particles reaches the capacity of the virtual microchannel, the enrichment enters the stable state (from 6 to 23 s). In this stage, while the nanoparticles from the upstream are continuously captured, the downstream particles are constantly scattered due to the strong interaction among the trapped nanoparticles. The scattered particles are represented by two red points in the detailed image. When the device is turned off, all particles leave the virtual microchannel and go downstream as shown in the image at 24 s.

As mentioned above, the virtual channel can self-adapt to different amounts of nanoparticles. The mechanism is that the interaction force (F_{int}) among the nanoparticles pushes the peripheral particles away from the virtual channel. Thus, the equilibrium position (wall of virtual channel) moves outward to a position with a higher acoustic pressure, establishing a new equilibrium, as shown in Fig. 4B. We then use the ID as a factor for evaluating the adaptivity of the virtual channel, whose boundary is defined by the distance between the positions where the normalized fluorescence was attenuated by 85%, as shown in fig. S8. Figure 4B shows that as the sample concentration increased, the ID expanded from 9 to 55 μm, which demonstrates that the virtual channel has more than 36 times the self-adaptivity in terms of capacity.

In addition to the channel spontaneously adapting to a large amount of nanoparticles, in situ enrichment is another important ability of the virtual channel, which means that it can be used to manipulate very dilute particles as well. We further analyzed the results of the in situ enrichment. Image processing software (MATLAB, USA) was used to produce the calibration curve of the nanoparticle concentration and the fluorescence intensity, as shown in fig. S9. The local concentration in the ROI after in situ enrichment was calculated by comparing the fluorescence value with the calibration curve. Figure S10 demonstrates that this platform has excellent performance in the in situ enrichment of nanoparticles at different concentrations ($n = 10$). Above the threshold concentration (0.75×10^{10} particles/ml for the 300-nm PS nanoparticles), the final enrichment concentration and the total amount of loaded nanoparticles increased with increasing applied power. Moreover, we used the concentration factor, which is defined by Eq. 1, to evaluate the enrichment performance

$$\alpha = C_{enrich}/C_{origin} \quad (1)$$

where α is the concentration factor, and C_{enrich} and C_{origin} denote the concentrations of the nanoparticles after and before enrichment. Different concentrations of 300-nm PS nanoparticles were enriched to a concentration of 10^{11}/ml, and the concentration factor was as

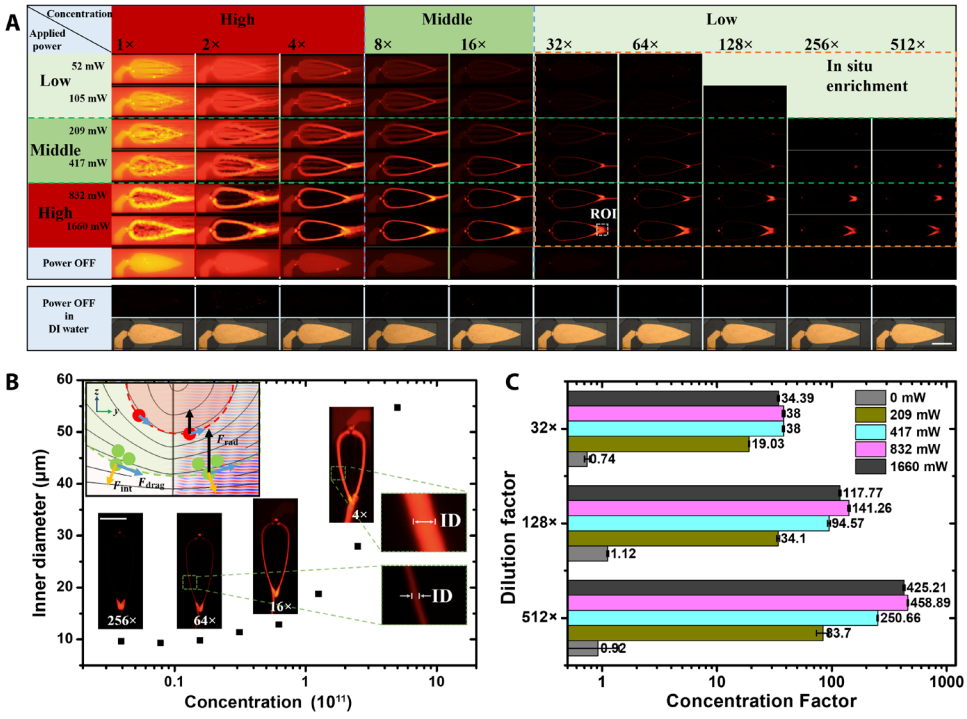

Fig. 4. Concentration adaptivity and in situ enrichment. (**A**) Concentration and applied power effects in the SteAS. All images were captured under the same observation conditions (lens, exposure time, exposure gain, and excitation light intensity). The diameter of the fluorescent PS particles was 300 nm. The images in the rectangular box below show the clean background in both the bright field and the fluorescent field when the nanoparticles are replaced by deionized (DI) water after each experiment. Scale bar, 200 μm. The ROI in the in situ enrichment is highlighted by a white dashed rectangle. (**B**) Self-adaptivity of the SteAS varies with the concentration. The ID of the virtual channel spontaneously expands as the sample concentration increases at a fixed applied power and flow rate. (**C**) Concentration factor of in situ enrichment at various applied powers and concentrations.

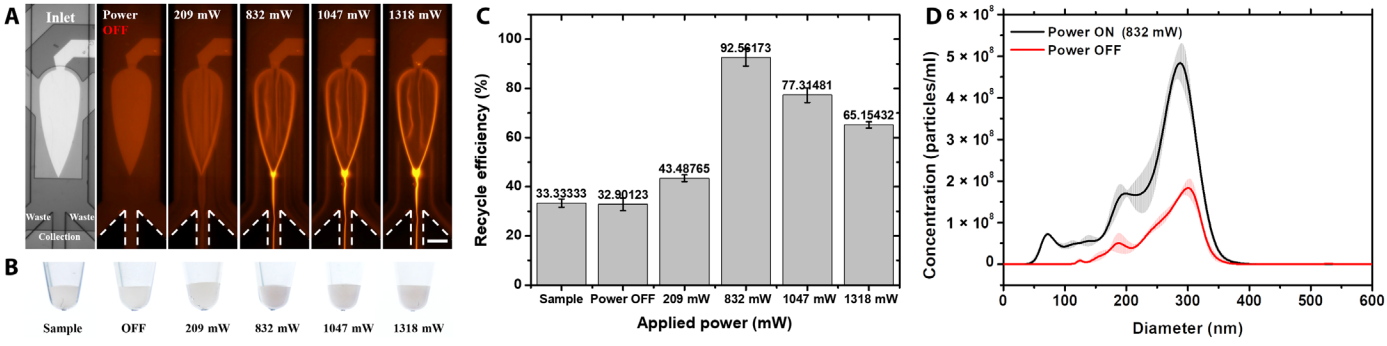

Fig. 5. Continuous focusing of nanoparticles. (**A**) Morphologies of continuous focusing at different applied powers. The diameter of the red fluorescent PS particles was 300 nm. The nanoparticles were focused and migrated with the virtual microchannel and released at the vertex of the gigahertz BAW device. Scale bar, 100 μm. (**B**) Images of the enriched samples at different applied powers recycled from the collection outlet. (**C**) Recycling efficiency calculated by the ratio of the total amount of enriched nanoparticles to the amount of injected nanoparticles. (**D**) Size distribution of the nanoparticles before and after continuous focusing.

high as 450 times, as shown in Fig. 4C. The results prove that the SteAS induced by Fan-BAW has an excellent enrichment performance that is sufficient for various biochemical applications. It is also worth noting that a clean background could be easily achieved by rinsing after each particle experiment. This indicates that the nanoparticles did not adhere to the channel even during long-term operations, which is difficult for conventional microfluidic systems without shear flow. This is due to the contactless handling mode of the virtual channel, which is crucial for the long-term processing of large amounts of nanoparticles.

Continuous focusing of nanoparticle

Continuous field flow fractionation (FFF)–based methods for particle manipulation have clear advantages, including device automation, high throughput, and easy integration with other downstream analyses (*51*). The focusing-type manipulation based on this virtual microchannel is well suited for nanoparticle pretreatment in continuous field flows. Continuous nanoparticle focusing, displacement, and release were achieved with the designed microfluidics, as shown in Fig. 5A and movie S8. Figure 5 (A and B) demonstrates the particle focusing phenomenon and the recovered samples from the center

outlet (the collection outlet) at different applied powers, respectively. The flow rate of the inlet was 3 μl/min, and the flow rate of all outlets (one recycled outlet and two waste outlets) was −1 μl/min (negative sign means that the pump is in the withdrawal mode). The figure shows that the focused samples are more turbid than the original samples. The concentrations of the focused and original samples were then quantified by nanoparticle tracking analysis (NTA; NS-300, Malvern) to determine the recovery efficiency, which was calculated by dividing the total amount of particles recovered from the recovery outlet by the total amount of particles injected into the microfluidic device, as shown in Fig. 5C. The total amount of nanoparticles was calculated by multiplying the concentration by the injection or collection volume. When the applied power was 832 mW, a recovery efficiency of 92.6% was achieved, which is extremely high for a continuous FFF-based nanoparticle manipulation microsystem (*12*). The relationship between the recovery efficiency and the applied power is consistent with the previous discussion, with the recovery efficiency first increasing and then decreasing as the applied power increased. The size distribution of the nanoparticles before and after enrichment is shown in Fig. 5D, indicating that the nanoparticles did not agglomerate and maintained good dispersion, which also proves the gentleness of this platform.

In SteAS-based focusing, the F_{rad} induced by traveling BAWs and the F_{drag} induced by acoustic streaming are the two major concerns and are both related to the size of the particles ($F_{rad} \propto r^3$ and $F_{drag} \propto r$). As the size of the particles decreases, the force that dominates the particle trajectory changes from the acoustic radiation force to the drag force; thus, the efficiency of focusing effect induced by the virtual channel depends on the size of the particles. To characterize the limit size of the continuous focusing mode, we focused 200-, 150-, and 100-nm PS nanoparticles in the continuous flow, as shown in Fig. 6 and movie S9. The results in Fig. 6 (A to C) showed the size distributions and concentration of nanoparticles before and after focusing under the same conditions. The focused samples were collected from the center outlet and quantified via NTA. The fluorescent images represented the morphologies of focusing process. Both NTA results and fluorescent images showed that the 200- and 150-nm nanoparticles were highly focused, while the 100-nm nanoparticles were not focused by the SteAS. The recovery efficiency was also calculated as the ratio of the total amount of nanoparticles after focusing to the total amount of nanoparticles before focusing. In this case, the recovery efficiency of the 200- and 150-nm nanoparticles reached 85.6 and 54.5%, respectively, while there was no notable enrichment effect on the 100-nm nanoparticles under this condition (Fig. 6D). This size-dependent continuous enrichment provides a theoretical basis for the separation of nanoparticles.

It is worth emphasizing that a higher recovery efficiency can be obtained by reducing the flow rate. However, such low flow rates cause the evaporation issue in the outlets, which makes it difficult to collect for NTA quantification. The fluorescence images of 150-nm nanoparticles before and after focusing at 0.6 and 0.3 μl/min are shown in fig. S11 (A and B). We extracted the fluorescent intensities of focused flows to qualitatively compare the recovery efficiencies of the two. The integral area of the intensities on the horizontal axis at the low flow rate is larger than that at the high flow rate, indicating that more nanoparticles are focused and higher recovery efficiency can be obtained at the low flow rate (fig. S11C). These results represent that the virtual microchannel maintains a continuous focusing capability for 150-nm PS nanoparticles.

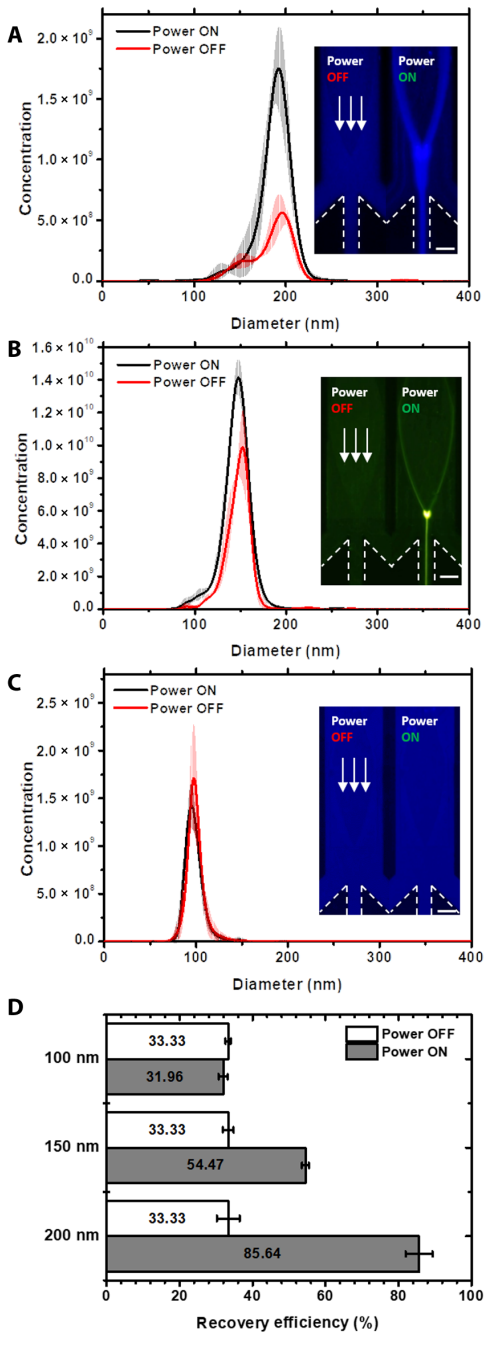

Fig. 6. Size-relative continuous focusing of nanoparticles. (**A** to **C**) Size distribution and concentration of the 200-, 150-, and 100-nm nanoparticles before and after continuous focusing. The images in the left show the morphologies of the focused fluorescent PS nanoparticles with the same parameters. The applied power was 1660 mW, and the height of the microchannel was 22 μm. The flow rate of the inlet was 0.6 μl/min, and the flow rates of the three outlets were all −0.2 μl/min. The white arrows point in the direction of the lateral flow. The boundaries of outlets are highlighted by white dashed lines. Scale bars, 100 μm. (**D**) Recovery efficiency of the 200-, 150-, and 100-nm nanoparticles after continuous focusing, which is calculated by the ratio of the total amount of focused nanoparticles (the middle outlet) to the amount of injected nanoparticles.

Focusing-type nanoparticle separation

To further verify the separation performance, we mixed 200-nm (blue) and 77-nm (red) fluorescent PS nanoparticles as the original sample for continuous separation experiments. In this part, the 77-nm particles were considered the separation target, while the 200-nm particles were considered impurities. On the basis of this, the center outlet was designed to be the waste outlet, while the outlets on both sides were designed as recovery outlets. Figure 7 (A and B) demonstrates the size distributions of the sample before and after separation, and the images show the focusing of the particles during the separation process when the BAW device was turned on/off. The separation process was recorded in movie S10. A cutoff diameter of 150 nm was chosen to calculate the purity of the sample before and after separation. After separation, the purity of the sample increased from 59.1 to 84.0%, demonstrating the good performance of this platform for purifying nanoparticles under 200 nm. It is worth noting that the particle concentration from the NTA measurement increased after separation. This phenomenon is most likely due to the overlaying effect of the intense light scattering of the large particles masking the smaller particles (*52*). Since the proportion of large particles was reduced after separation, the scattered light of the small particles that were originally masked could be observed, which may cause a "false increase" in their concentration.

To verify the performance of this platform in actual clinical samples, we used this system to perform exosome separation in plasma samples. Exosomes are nanoscale EVs found in nearly all biological fluids, including blood, urine, sputum, and cerebrospinal fluid (*53*). Different from microvesicles (MVs; another kind of EVs), whose diameter ranges from 100 to 2000 nm, the diameter of exosomes ranges from 30 to 150 nm. Such small size makes its purification difficult (*54*). However, they have been identified as potential biomarkers for health monitoring and diagnosis in recent years (*16*, *23*). Since the SteAS was verified to have excellent performance in the manipulation of 200-nm nanoparticles, we used this platform to purify exosomes directly from human plasma, which contains different sized mixtures of cell debris, MVs, proteins, DNAs, and lipids. Undiluted human plasma samples from a cancer patient were used as the original sample. The setup was the same as that demonstrated above; the outlets on both sides were the recovery outlets, while the center outlet was the waste outlet. The stacked images (80 frames) of the focusing phenomenon are shown in Fig. 8A, and the process of MVs focusing is demonstrated in movie S11. When the device was turned off, the MVs, which are highlighted by black arrows, were randomly distributed in the microchannel and flowed downstream along the lateral flow direction. When the device was turned on, the MVs were rapidly trapped and focused in the virtual channel and then released at the vertex of the device; the focused MVs are highlighted by a white arrow. The Western blot analysis was used to examine the expression of exosomal protein markers. We analyzed the expression of EV membrane tetraspanins CD63 and CD81 in the sample collected from the recovery outlets on both sides and the blood plasma, as shown in Fig. 8B. The isolated exosomes showed a high expression of CD63 and CD81, confirming the presence of exosomes in the samples. These proteins were also present in the original plasma samples, as expected. NTA was also used to characterize the size distribution of the original sample and the purified sample, as shown in Fig. 8 (C and D). Three independent tests were performed for each sample, and the raw data are shown in fig. S12. After separation, the 169-nm MVs in the original sample were efficiently removed, demonstrating the excellent separation resolution of the platform. To reduce the detection error caused by the overlapping effect, the sample was diluted by a high multiple (500×) to ensure that there were approximately 100 particles per frame during the NTA test (*52*). Because of the high dilution factor, it is difficult to detect large EVs with a small sample size. We speculate that this may be the reason why the EVs observed by the microscope were not reflected in the NTA results. Transmission electron microscopy (TEM) (HT7700, Hitachi, Japan) was used to characterize the morphology of the exosomes before and after stimulation. The exosomes actuated by the SteAS at 832 and 1660 mW maintained the same morphology as the exosomes without stimulation, as shown in fig. S13. The results verify the high separation resolution and good biocompatibility of this platform in the size-based separation of soft nanoparticles.

DISCUSSION

We demonstrated a new active strategy for continuous nanoparticle manipulation based on a virtual microchannel that combines

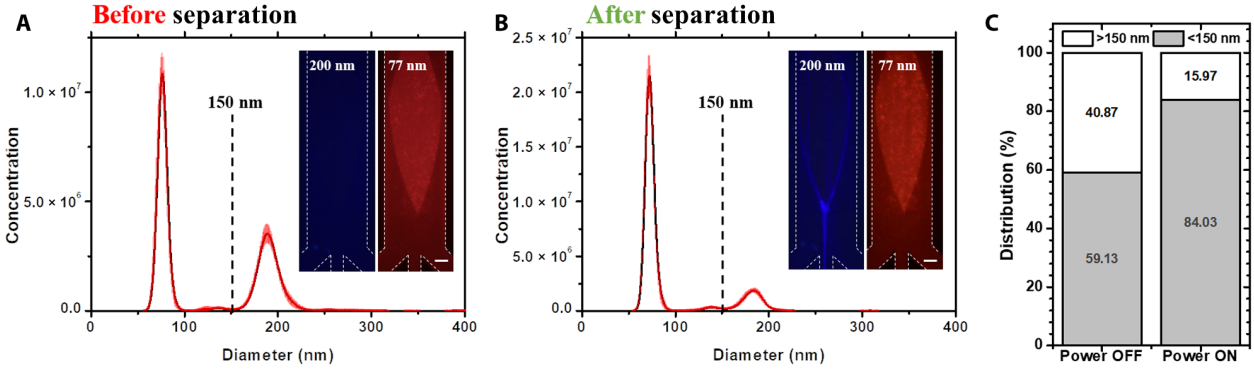

Fig. 7. Focusing-type separation of nanoparticles via SteAS. (**A** and **B**) Size distributions of the mixed nanoparticles before and after focusing-type separation. The mixed sample consisted of 77-nm (red) and 200-nm (blue) PS nanoparticles. The cutoff diameter (150 nm) is highlighted by a black dashed line. The images on the left show the morphologies of the 77- and 200-nm nanoparticles during the separation process. The applied power was 1660 mW. The flow rate of the inlet was 1.5 μl/min, and the flow rates of the three outlets were −0.5 μl/min. The height of the microchannel was 30 μm. The purified samples were collected from the outlets on both sides. Scale bars, 100 μm. (**C**) Purity of the samples before and after separation. The purity is defined by the percentage of nanoparticles under 150 nm. The proportion of 77-nm nanoparticles increased from 59.13 to 84.03%.

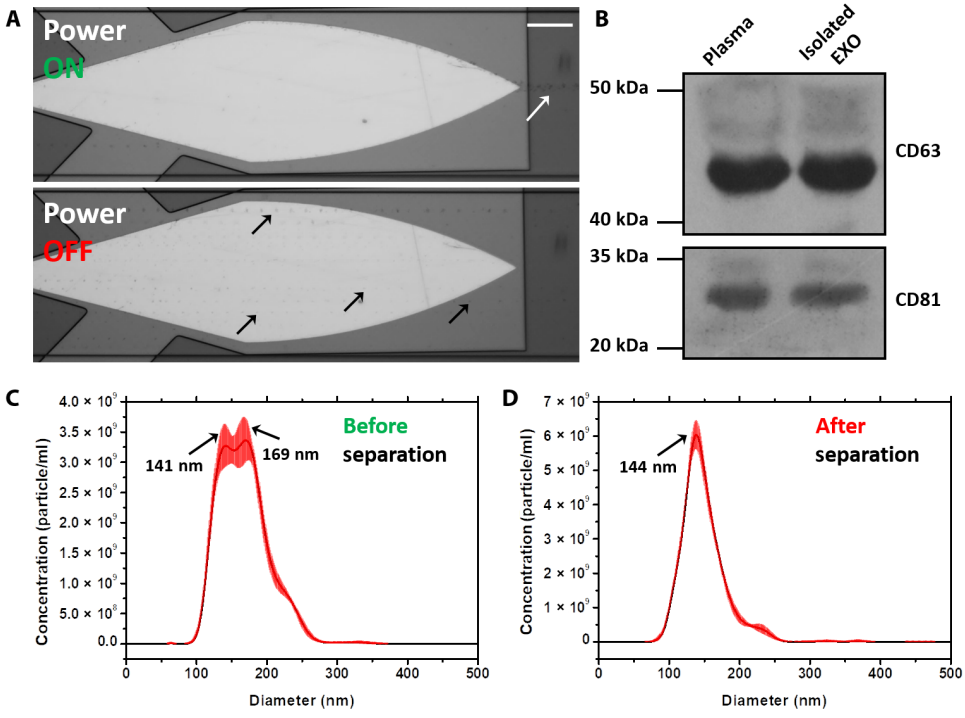

Fig. 8. Focusing-type separation of exosomes from patient plasma. (**A**) Stacked images of MVs when the device was off/on. The images are stacked by 80 frames and show the trajectories of the MVs before (black arrows) and after (white arrow) focusing. The height of the microchannel was 50 μm. The flow rate of the inlet was 0.6 μl/min, and the flow rates of the three outlets were −0.2 μl/min. Scale bar, 100 μm. (**B**) Western blot analysis of the sample collected from exosome outlets (Isolated EXO) and plasma, showing a prominent expression of exosomal protein markers in the isolated exosome and blood samples. (**C** and **D**) Size distribution of the EVs before and after separation. The peaks are highlighted by arrows.

hydrodynamic and acoustic features and is induced by an innovatively designed BAW resonator. Because of the unique device shape design, the acoustic stream has a distinct spatial distribution that is orthogonal to the vector of the lateral flow, which minimizes the interaction while maximizing the focusing performance. Because of the action of the acoustic radiation force and the drag force, the particles are focused in the center of the vortices with a helical trajectory in the axial plane. In addition, the ultrahigh frequency (>1 GHz) increases the strength of the acoustic stream and shortens the attenuation length, allowing for a more confined environment that enhances the intensity of the radiation force.

On the basis of experiments and numerical simulations, we demonstrated the in situ enrichment of nanoparticles as small as 30 nm and the continuous focusing and migration of 150-nm PS nanoparticles. Because of the self-adaptivity of SteAS, the nanoparticles are stably trapped in the vortices during their migration inside the virtual channel, even under strong interaction conditions, which enables continuous focusing-type nanoparticle enrichment and separation. As a proof of concept, the purification of exosomes from patient plasma was also achieved. Because of the label-free, contactless, and self-adaptive continuous separation mode, this system has high automation potential and good stability for the long-term processing of nanospecimens, even with uncertain samples. Compared with other existing nanoparticle manipulation techniques, the virtual microchannel technology, as an unbiased separation method, has advantages in the optional handling mode, powerful enrichment capability, and high recovery efficiency (see table S1 for the comparison of different nanoparticle enrichment and focusing techniques). Furthermore, as the device is CMOS compatible, multiple devices with different designs and scales can be fabricated on the same chip to meet the requirements of various application scenarios. For example, to achieve more dedicated particle separation with multiple steps for complex samples, multiple acoustic devices with different applied powers could be cascaded in one system. One of the limitations of the system is the throughput to focus nanoparticles less than 150 nm. Although we have demonstrated the in situ enrichment of 30-nm nanoparticles and continuous focusing of 150-nm nanoparticles, it took several minutes to achieve sufficient accumulation and maintain good performance at low flow rates, which are insufficient for sample pretreatment with high-throughput requirements. This could be improved by increasing the acoustic frequency to enhance the strength of the SteAS, as well as parallel processing using multiple channels integrated with more devices. In addition, the microfluidic technology in this system allows for controllable fluid drive and material transport. Thus, by combining the SteAS and multiphase lateral flow, this platform has the potential to achieve a variety of nanoparticle manipulations, such as washing, synthesis, and immune labeling of nanoparticles, matching more complex scenarios.

To better understand the mechanism and improve the performance, we systematically discussed the effects of various internal and external factors on microvortex control, including the morphology of the microfluidic channel (height and structure), the specimen characteristics (size and concentration), and the device parameters (shape, resonant frequency, applied power, flow rates, and vortex distribution). Although the theoretical analysis and simulations illustrate the relationship between the vortex distribution and the shape of

the gigahertz BAW device and clarify the effect of the microchannel height, we cannot directly calculate the effects of these factors on the nanoparticle focus because of the lack of a quantitative relationship between gigahertz BAWs and the radiation force acting on the nanoparticles. To the best of our knowledge, there are two strategies for determining the acoustic radiation force: building a quantitative relationship between the applied power and the resultant substrate velocity amplitude via laser Doppler vibrometry (*55*) or calculating the quantitative relationship based on the particle trajectory under the decoupled action of the radiation force (*56*). However, due to the ultrahigh frequency and its coupling with the drag force induced by the acoustic vortices, neither of these strategies is suitable for our system. Understanding the mechanism and decoupling the effects of various factors are important directions that could lead to a more efficient system in the future.

In summary, we developed a continuous fraction system in which a virtual dynamic microchannel formed by acoustic waves and streaming efficiently enriched, focused, and separated nanoparticles. The new design principle based on SteAS continuity improved platform performance and enriched the technical library of acoustofluidics. We believe that this novel platform can bridge the gap between microfluidics and nanoscale specimen manipulation, and that it is a promising tool for simplifying pretreatment, accelerating detection, and automating reactions in biology, medicine, and chemistry.

MATERIALS AND METHODS

Device design, fabrication, and operation

The gigahertz BAW device was designed with finite element simulation software (COMSOL, USA) based on the principle mentioned in the article and fabricated as described in a previous publication (*43*). In terms of thickness, the device can be divided into two parts: the Bragg mirror structure, which consists of alternating layers of silicon dioxide (SiO_2) and aluminum nitride (AlN) deposited on a silicon substrate for BAW reflection, and the sandwich structure, which consists of molybdenum (Mo), AlN, and gold (Au) as the bottom electrode (BE), piezoelectric layer, and top electrode (TE) for acoustic vibration, as shown in fig. S3. The differently colored regions in the device image are due to the different patterned electrodes, and the outlines of the BE and TE are depicted with green and blue dashed lines, respectively. The Bragg reflector layer and the piezoelectric layer cover the entire silicon substrate. The area where the TE and BE overlap is the actual vibration area of the UHF BAW device. First, the film thickness for a vibration frequency of 2 GHz was calculated by the following equation

$$f_n = (2n+1)\cdot\frac{v^D}{4d}, n = 0, 1, 2, \ldots \quad (2)$$

where f_n is the nth-order parallel resonant frequency of the BAW device, n is the number of orders, v^D is the acoustic velocity within the piezoelectric layer, and d is the half thickness of the piezoelectric film.

The photo of the setup is shown in fig. S2. Briefly, the gigahertz BAW device was actuated by a sinusoidal signal (2 GHz) generated by a signal generator (Agilent, N5171b) and amplified by a power amplifier (Mini-Circuits, ZHL-5 W-422+). Because of the inverse piezoelectric effect, the piezoelectric layer vibrates in the thickness extension mode, which is driven by a sinusoidal signal on the BE and TE layer. The injection flow and withdraw flow were individually controlled by syringe pumps (Harvard, 704504). The SteAS platform was placed on an upright microscope (BX53, Olympus). A charge-coupled device camera (DP73, Olympus) was used to record the manipulation process in the *x-y* plane. A confocal microscope (Leica, SP8) was used to observe the spatial distribution of the SteAS in the microchannel. The *x-y-z* and *x-z-t* modes with a super-z stage were used to record the steady state of the nanoparticles enriched in the center of the vortices as well as the trajectories and movement of the nanoparticles in the axial plane.

The microfluidic channel was fabricated by a standard soft lithography process based on polydimethylsiloxane (PDMS). A thin layer of SU-8 photoresist (Microchem, USA) was spin-coated and patterned by ultraviolet exposure on a silicon wafer. The PDMS base and curing agent (Dow Corning, USA) were mixed in a 10:1 ratio, poured into the SU-8 mold, and cured at 65°C for 45 min. Then, the microchannel was peeled off the mold and cut into the desired shape. A metal punch was used to drill holes in the channel to form the inlets and outlets. Last, the PDMS microchannel was integrated with the BAW device with a customized holder. More details about the structure of this device can be found in fig. S2.

Sample preparation

PS nanoparticles of 300, 200, 150, 100, 77, and 30 nm (Aladdin, China; Beijing Dk Nano Technology, China; Huge Biotechnology, China; Sigma-Aldrich, USA) with different fluorescence tags were used in the experiments. The size distribution and concentration of these nanoparticles were characterized by NTA. Single dispersed samples were obtained by diluting the primary nanoparticle samples. The diluted nanoparticles (300 nm) were obtained by dilution in equal proportions (1×, 2×, 4×, …, 256×, 512×). The original concentration of 300-nm PS nanoparticles tested by NTA (NS-300, Malvern) was 1.02×10^{12} particles/ml. The mixed samples were prepared by combining nanoparticles of two different sizes. The principle of mixed sample preparation is to ensure that the concentrations of the two nanoparticles in the final samples were similar, allowing two clear peaks to be seen during the NTA. The concentration of the final nanoparticle samples was about 1×10^8 particles/ml.

Human plasma was obtained from Tianjin Medical University Cancer Institute & Hospital and stored at −20°C. Exosome samples were isolated and enriched from a cell culture buffer using ultracentrifugation. H520 cell culture buffer (60 ml) was obtained from Tianjin Medical University Cancer Institute & Hospital. The procedure followed the existing protocols (*57*).

Image analysis

The microscope images and video were analyzed by MATLAB R2015a (MathWorks, USA). We used the software to automatically extract the fluorescence value in the ROIs in batches. The pre- and postprocessed exosome samples were collected and visualized using TEM and a negative staining method.

Characterization of sample

The size distribution and concentration of the nanoparticles before and after treatment were characterized by NTA. Each NTA video was 60 s, and each result was averaged by at least three tests. The concentration of the preprocessed polydisperse sample in the NTA test was diluted to guarantee that there were 70 to 120 particles per frame to ensure statistics and suppress the overlapping

effect. For monodisperse samples, at least 10 particles per frame were guaranteed.

For protein extraction and Western blot, plasma samples were lysed with lysis buffer and subjected to 10% SDS–polyacrylamide gel electrophoresis gels and transferred to a polyvinylidene difluoride membrane. Anti-CD63 (1:200; Santa Cruz Biotechnology) and anti-CD81 (1:200; Santa Cruz Biotechnology) antibodies were used as primary antibodies to confirm the presence of exosomes. The bound primary antibody was detected by peroxidase-conjugated goat anti-rabbit immunoglobulin G (Sigma-Aldrich) and the ECL Western blot analysis system (Millipore). Each experiment was performed at least three times.

Finite element simulation

The simulation of the vibration of the gigahertz BAW device was realized by COMSOL Multiphysics 5.5. The thickness of the piezoelectric layer was calculated by Eq. 2. The electrostatics module, solid mechanics module, and multiphysics module (piezoelectric effect) were used in the vibration modeling. The 3D simulation results of the vibration mode are shown in Fig. 1B. The SteAS model was simulated by the laminar flow module in a microscale space. The gigahertz BAWs and the fluids were coupled by a decaying body force triggered by the attenuation of the acoustic waves, which was calculated by Eq. 3 (*48*)

$$F_{\text{body}} = 2\beta\rho\, v_0^2 e^{-2\beta z} \tag{3}$$

where β, ρ, v_0, z, and e denote the attenuation coefficient, the density of the liquid, the initial velocity amplitude, the propagation direction, and the natural base. The attenuation coefficient is defined by

$$\beta = \frac{\omega^2}{2\rho c_l^3}\left(\frac{4}{3}\mu + \mu_B\right) \tag{4}$$

where ω, c_l, ρ, μ, and μ_B are the angular frequency, sound speed in liquid, density, dynamic viscosity, and bulk viscosity of liquid, respectively. The area where the body force acted coincided with the area of the BAW device. The laminar flow module was set to be incompressible, and the fluid medium was water. The boundaries of the microchannel were set to nonslip walls, and the inlet and outlet were set to open borders.

SUPPLEMENTARY MATERIALS

Supplementary material for this article is available at https://science.org/doi/10.1126/sciadv.abn8440

REFERENCES AND NOTES

1. J. Li, B. E.-F. de Ávila, W. Gao, L. Zhang, J. Wang, Micro/nanorobots for biomedicine: Delivery, surgery, sensing, and detoxification. *Sci. Robot.* **2**, eaam6431 (2017).
2. S. Zhang, C. Chen, C. Xue, D. Chang, H. Xu, B. J. Salena, Y. Li, Z. S. Wu, Ribbon of DNA lattice on gold nanoparticles for selective drug delivery to cancer cells. *Angew. Chem. Int. Ed. Engl.* **59**, 14584–14592 (2020).
3. M. Li, T. Lohmuller, J. Feldmann, Optical injection of gold nanoparticles into living cells. *Nano Lett.* **15**, 770–775 (2015).
4. M. Poudineh, P. M. Aldridge, S. Ahmed, B. J. Green, L. Kermanshah, V. Nguyen, C. Tu, R. M. Mohamadi, R. K. Nam, A. Hansen, S. S. Sridhar, A. Finelli, N. E. Fleshner, A. M. Joshua, E. H. Sargent, S. O. Kelley, Tracking the dynamics of circulating tumour cell phenotypes using nanoparticle-mediated magnetic ranking. *Nat. Nanotechnol.* **12**, 274–281 (2017).
5. J. Sun, Y. Xianyu, X. Jiang, Point-of-care biochemical assays using gold nanoparticle-implemented microfluidics. *Chem. Soc. Rev.* **43**, 6239–6253 (2014).
6. J. Huang, F. Kim, A. R. Tao, S. Connor, P. Yang, Spontaneous formation of nanoparticle stripe patterns through dewetting. *Nat. Mater.* **4**, 896–900 (2005).
7. H. Wang, Y. Zhang, B. Huang, W. Deng, Y. Quan, W. Wang, W. Xu, Y. Zhao, N. Li, J. Zhang, H. Liang, L. Bao, Y. Xu, L. Ding, W. Zhou, H. Gao, J. Liu, P. Niu, L. Zhao, W. Zhen, H. Fu, S. Yu, Z. Zhang, G. Xu, C. Li, Z. Lou, M. Xu, C. Qin, G. Wu, G. F. Gao, W. Tan, X. Yang, Development of an inactivated vaccine candidate, BBIBP-CorV, with potent protection against SARS-CoV-2. *Cell* **182**, 713–721.e9 (2020).
8. R. Drmanac, A. B. Sparks, M. J. Callow, A. L. Halpern, N. L. Burns, B. G. Kermani, P. Carnevali, I. Nazarenko, G. B. Nilsen, G. Yeung, F. Dahl, A. Fernandez, B. Staker, K. P. Pant, J. Baccash, A. P. Borcherding, A. Brownley, R. Cedeno, L. Chen, D. Chernikoff, A. Cheung, R. Chirita, B. Curson, J. C. Ebert, C. R. Hacker, R. Hartlage, B. Hauser, S. Huang, Y. Jiang, V. Karpinchyk, M. Koenig, C. Kong, T. Landers, C. Ie, J. Liu, C. E. McBride, M. Morenzoni, R. E. Morey, K. Mutch, H. Perazich, K. Perry, B. A. Peters, J. Peterson, C. L. Pethiyagoda, K. Pothuraju, C. Richter, A. M. Rosenbaum, S. Roy, J. Shafto, U. Sharanhovich, K. W. Shannon, C. G. Sheppy, M. Sun, J. V. Thakuria, A. Tran, D. Vu, A. W. Zaranek, X. Wu, S. Drmanac, A. R. Oliphant, W. C. Banyai, B. Martin, D. G. Ballinger, G. M. Church, C. A. Reid, Human genome sequencing using unchained base reads on self-assembling DNA nanoarrays. *Science* **327**, 78–81 (2010).
9. P. Zhang, X. Zhou, M. He, Y. Shang, A. L. Tetlow, A. K. Godwin, Y. Zeng, Ultrasensitive detection of circulating exosomes with a 3D-nanopatterned microfluidic chip. *Nat. Biomed. Eng.* **3**, 438–451 (2019).
10. C. Liu, J. Zhao, F. Tian, L. Cai, W. Zhang, Q. Feng, J. Chang, F. Wan, Y. Yang, B. Dai, Y. Cong, B. Ding, J. Sun, W. Tan, Low-cost thermophoretic profiling of extracellular-vesicle surface proteins for the early detection and classification of cancers. *Nat. Biomed. Eng.* **3**, 183–193 (2019).
11. Z. Zhao, J. Fan, Y. M. S. Hsu, C. J. Lyon, B. Ning, T. Y. Hu, Extracellular vesicles as cancer liquid biopsies: From discovery, validation, to clinical application. *Lab Chip* **19**, 1114–1140 (2019).
12. Y. Xie, J. Rufo, R. Zhong, J. Rich, P. Li, K. W. Leong, T. J. Huang, Microfluidic isolation and enrichment of nanoparticles. *ACS Nano* **14**, 16220–16240 (2020).
13. X. Duan, Y. Li, Physicochemical characteristics of nanoparticles affect circulation, biodistribution, cellular internalization, and trafficking. *Small* **9**, 1521–1532 (2013).
14. F. Zhao, Y. Zhao, Y. Liu, X. Chang, C. Chen, Y. Zhao, Cellular uptake, intracellular trafficking, and cytotoxicity of nanomaterials. *Small* **7**, 1322–1337 (2011).
15. H. Zhang, D. Lyden, Asymmetric-flow field-flow fractionation technology for exomere and small extracellular vesicle separation and characterization. *Nat. Protoc.* **14**, 1027–1053 (2019).
16. H. Shao, H. Im, C. M. Castro, X. Breakefield, R. Weissleder, H. Lee, New technologies for analysis of extracellular vesicles. *Chem. Rev.* **118**, 1917–1950 (2018).
17. Z. Zhao, Y. Yang, Y. Zeng, M. He, A microfluidic ExoSearch chip for multiplexed exosome detection towards blood-based ovarian cancer diagnosis. *Lab Chip* **16**, 489–496 (2016).
18. F. A. W. Coumans, A. R. Brisson, E. I. Buzas, F. Dignat-George, E. E. E. Drees, S. el-Andaloussi, C. Emanueli, A. Gasecka, A. Hendrix, A. F. Hill, R. Lacroix, Y. Lee, T. G. van Leeuwen, N. Mackman, I. Mäger, J. P. Nolan, E. van der Pol, D. M. Pegtel, S. Sahoo, P. R. M. Siljander, G. Sturk, O. de Wever, R. Nieuwland, Methodological guidelines to study extracellular vesicles. *Circ. Res.* **120**, 1632–1648 (2017).
19. V. Sunkara, H. K. Woo, Y. K. Cho, Emerging techniques in the isolation and characterization of extracellular vesicles and their roles in cancer diagnostics and prognostics. *Analyst* **141**, 371–381 (2016).
20. F. Liu, O. Vermesh, V. Mani, T. J. Ge, S. J. Madsen, A. Sabour, E. C. Hsu, G. Gowrishankar, M. Kanada, J. V. Jokerst, R. G. Sierra, E. Chang, K. Lau, K. Sridhar, A. Bermudez, S. J. Pitteri, T. Stoyanova, R. Sinclair, V. S. Nair, S. S. Gambhir, U. Demirci, The exosome total isolation chip. *ACS Nano* **11**, 10712–10723 (2017).
21. M. Wu, A. Ozcelik, J. Rufo, Z. Wang, R. Fang, T. Jun Huang, Acoustofluidic separation of cells and particles. *Microsyst. Nanoeng.* **5**, 32 (2019).
22. Y. T. Yeh, Y. Tang, A. Sebastian, A. Dasgupta, N. Perea-Lopez, I. Albert, H. Lu, M. Terrones, S. Y. Zheng, Tunable and label-free virus enrichment for ultrasensitive virus detection using carbon nanotube arrays. *Sci. Adv.* **2**, e1601026 (2016).
23. M. Wu, Y. Ouyang, Z. Wang, R. Zhang, P. H. Huang, C. Chen, H. Li, P. Li, D. Quinn, M. Dao, S. Suresh, Y. Sadovsky, T. J. Huang, Isolation of exosomes from whole blood by integrating acoustics and microfluidics. *Proc. Natl. Acad. Sci. U.S.A.* **114**, 10584–10589 (2017).
24. A. Ku, H. C. Lim, M. Evander, H. Lilja, T. Laurell, S. Scheding, Y. Ceder, Acoustic enrichment of extracellular vesicles from biological fluids. *Anal. Chem.* **90**, 8011–8019 (2018).
25. L. Lin, Q. Chen, J. Sun, Micro/nanofluidics-enabled single-cell biochemical analysis. *TrAC Trends Analyt. Chem.* **99**, 66–74 (2018).
26. Y. Zhou, Z. Ma, M. Tayebi, Y. Ai, Submicron particle focusing and exosome sorting by wavy microchannel structures within viscoelastic fluids. *Anal. Chem.* **91**, 4577–4584 (2019).
27. T. Salafi, K. K. Zeming, Y. Zhang, Advancements in microfluidics for nanoparticle separation. *Lab Chip* **17**, 11–33 (2016).
28. Z. Han, J. Liu, Z. Liu, W. Pan, Y. Yang, X. Chen, Y. Gao, X. Duan, Resistive pulse sensing device with embedded nanochannel (nanochannel-RPS) for label-free biomolecule and bionanoparticle analysis. *Nanotechnology* **32**, 295507 (2021).

29. S. H. Ko, D. Chandra, W. Ouyang, T. Kwon, P. Karande, J. Han, Nanofluidic device for continuous multiparameter quality assurance of biologics. *Nat. Nanotechnol.* **12**, 804–812 (2017).
30. B. H. Wunsch, J. T. Smith, S. M. Gifford, C. Wang, M. Brink, R. L. Bruce, R. H. Austin, G. Stolovitzky, Y. Astier, Nanoscale lateral displacement arrays for the separation of exosomes and colloids down to 20 nm. *Nat. Nanotechnol.* **11**, 936–940 (2016).
31. C. Liu, J. Guo, F. Tian, N. Yang, F. Yan, Y. Ding, J. Y. Wei, G. Hu, G. Nie, J. Sun, Field-free isolation of exosomes from extracellular vesicles by microfluidic viscoelastic flows. *ACS Nano* **11**, 6968–6976 (2017).
32. S. D. Ibsen, J. Wright, J. M. Lewis, S. Kim, S. Y. Ko, J. Ong, S. Manouchehri, A. Vyas, J. Akers, C. C. Chen, B. S. Carter, S. C. Esener, M. J. Heller, Rapid isolation and detection of exosomes and associated biomarkers from plasma. *ACS Nano* **11**, 6641–6651 (2017).
33. D. Psaltis, S. R. Quake, C. Yang, Developing optofluidic technology through the fusion of microfluidics and optics. *Nature* **442**, 381–386 (2006).
34. Z. Mao, P. Li, M. Wu, H. Bachman, N. Mesyngier, X. Guo, S. Liu, F. Costanzo, T. J. Huang, Enriching nanoparticles via acoustofluidics. *ACS Nano* **11**, 603–612 (2017).
35. P. Li, T. J. Huang, Applications of acoustofluidics in bioanalytical chemistry. *Anal. Chem.* **91**, 757–767 (2019).
36. Y. Gu, C. Chen, J. Rufo, C. Shen, Z. Wang, P. H. Huang, H. Fu, P. Zhang, S. A. Cummer, Z. Tian, T. J. Huang, Acoustofluidic holography for micro- to nanoscale particle manipulation. *ACS Nano* **14**, 14635–14645 (2020).
37. P. Zhang, J. Rufo, C. Chen, J. Xia, Z. Tian, L. Zhang, N. Hao, Z. Zhong, Y. Gu, K. Chakrabarty, T. J. Huang, Acoustoelectronic nanotweezers enable dynamic and large-scale control of nanomaterials. *Nat. Commun.* **12**, 3844 (2021).
38. M. Tayebi, D. Yang, D. J. Collins, Y. Ai, Deterministic sorting of submicrometer particles and extracellular vesicles using a combined electric and acoustic field. *Nano Lett.* **21**, 6835–6842 (2021).
39. D. J. Collins, Z. Ma, J. Han, Y. Ai, Continuous micro-vortex-based nanoparticle manipulation via focused surface acoustic waves. *Lab Chip* **17**, 91–103 (2017).
40. D. J. Collins, Z. Ma, Y. Ai, Highly localized acoustic streaming and size-selective submicrometer particle concentration using high frequency microscale focused acoustic fields. *Anal. Chem.* **88**, 5513–5522 (2016).
41. Z. Chen, P. Liu, X. Zhao, L. Huang, Y. Xiao, Y. Zhang, J. Zhang, N. Hao, Sharp-edge acoustic microfluidics: Principles, structures, and applications. *Appl. Mater. Today* **25**, 101239 (2021).
42. K. Kolesnik, M. Xu, P. V. S. Lee, V. Rajagopal, D. J. Collins, Unconventional acoustic approaches for localized and designed micromanipulation. *Lab Chip* **21**, 2837–2856 (2021).
43. W. Cui, H. Zhang, H. Zhang, Y. Yang, M. He, H. Qu, W. Pang, D. Zhang, X. Duan, Localized ultrahigh frequency acoustic fields induced micro-vortices for submilliseconds microfluidic mixing. *Appl. Phys. Lett.* **109**, 253503 (2016).
44. H. Qu, Y. Yang, Y. Chang, Z. Tang, W. Pang, Y. Wang, H. Zhang, X. Duan, On-chip integrated multiple microelectromechanical resonators to enable the local heating, mixing and viscosity sensing for chemical reactions in a droplet. *Sens. Actuators B Chem.* **248**, 280–287 (2017).
45. W. Pang, H. Zhao, E. S. Kim, H. Zhang, H. Yu, X. Hu, Piezoelectric microelectromechanical resonant sensors for chemical and biological detection. *Lab Chip* **12**, 29–44 (2012).
46. W. Cui, M. He, Y. Yang, H. Zhang, W. Pang, X. Duan, Hypersonic-induced 3D hydrodynamic tweezers for versatile manipulations of micro/nanoscale objects. *Part. Part. Syst. Charact.* **35**, 1800068 (2018).
47. R. Jiang, S. Agrawal, M. Aghaamoo, R. Parajuli, A. Agrawal, A. P. Lee, Rapid isolation of circulating cancer associated fibroblasts by acoustic microstreaming for assessing metastatic propensity of breast cancer patients. *Lab Chip* **21**, 875–887 (2021).
48. X. Guo, M. Sun, Y. Yang, H. Xu, J. Liu, S. He, Y. Wang, L. Xu, W. Pang, X. Duan, Controllable cell deformation using acoustic streaming for membrane permeability modulation. *Adv. Sci.* **8**, 2002489 (2021).
49. Y. Gu, C. Chen, Z. Mao, H. Bachman, R. Becker, J. Rufo, Z. Wang, P. Zhang, J. Mai, S. Yang, J. Zhang, S. Zhao, Y. Ouyang, D. T. W. Wong, Y. Sadovsky, T. J. Huang, Acoustofluidic centrifuge for nanoparticle enrichment and separation. *Sci. Adv.* **7**, eabc0467 (2021).
50. S. Pan, H. Zhang, W. Liu, Y. Wang, W. Pang, X. Duan, Biofouling removal and protein detection using a hypersonic resonator. *ACS Sens.* **2**, 1175–1183 (2017).
51. M. Wu, Z. Mao, K. Chen, H. Bachman, Y. Chen, J. Rufo, L. Ren, P. Li, L. Wang, T. J. Huang, Separation: Acoustic separation of nanoparticles in continuous flow. *Adv. Funct. Mater.* **27**, 1606039 (2017).
52. R. Szatanek, M. Baj-Krzyworzeka, J. Zimoch, M. Lekka, M. Siedlar, J. Baran, The methods of choice for extracellular vesicles (EVs) characterization. *Int. J. Mol. Sci.* **18**, 1153 (2017).
53. N. Cheng, D. du, X. Wang, D. Liu, W. Xu, Y. Luo, Y. Lin, Recent advances in biosensors for detecting cancer-derived exosomes. *Trends Biotechnol.* **37**, 1236–1254 (2019).
54. S. Gurunathan, M. H. Kang, M. Jeyaraj, M. Qasim, J. H. Kim, Review of the isolation, characterization, biological function, and multifarious therapeutic approaches of exosomes. *Cell* **8**, 307 (2019).
55. D. J. Collins, A. Neild, Y. Ai, Highly focused high-frequency travelling surface acoustic waves (SAW) for rapid single-particle sorting. *Lab Chip* **16**, 471–479 (2016).
56. D. Hartono, Y. Liu, P. L. Tan, X. Y. S. Then, L. Y. L. Yung, K. M. Lim, On-chip measurements of cell compressibility via acoustic radiation. *Lab Chip* **11**, 4072–4080 (2011).
57. C. Thery, S. Amigorena, G. Raposo, A. Clayton, Isolation and characterization of exosomes from cell culture supernatants and biological fluids. *Curr. Protoc. Cell Biol.* **Chapter 3**, Unit 3.22 (2006).

Acknowledgments: We acknowledge the support from H. Jiao (Tianjin Medical University) in the TEM imaging and H. Yin and Yin's group (Tianjin Medical University) for the Western blot analysis. Y.Y. thanks H. Li for company and support. Y.Y. also acknowledges financial support from the Zhejiang Lab's International Talent Fund for Young Professionals. **Funding:** We acknowledge financial support from the National Key R&D Program of China (2018YFE0118700), the Natural Science Foundation of China (NSFC no. 62174119), Tianjin Applied Basic Research and Advanced Technology (17JCJQJC43600), and the 111 Project (B07014). **Author contributions:** Conceptualization: Y.Y. and X.D. Methodology: Y.Y., M.H., K.J., Q.Y., L.Z., and X.R. Investigation: Y.Y., W.W., X.C., Y.W., and W.P. Visualization: Y.Y. Supervision: X.D. Writing—original draft: Y.Y. Writing—review and editing: Y.Y. and X.D. **Competing interests:** The authors declare that they have no competing interests. **Data and materials availability:** All data needed to evaluate the conclusions in the paper are present in the paper and/or the Supplementary Materials.

Submitted 26 January 2022
Accepted 14 June 2022
Published 29 July 2022
10.1126/sciadv.abn8440